NAFEMS WORLD CONGRESS 2015 – ANALYSIS AND VERIFICATION APPROACH FOR DESIGN OF A LIGHTWEIGHT ORION HEAT SHIELD CARRIER STRUCTURE

Eric Gustafson, Jim Jeans
(Structural Design and Analysis, Inc., USA);

James Ainsworth
(Collier Research Corp., USA);

ANALYSIS AND VERIFICATION APPROACH FOR DESIGN OF A LIGHTWEIGHT ORION HEAT SHIELD CARRIER STRUCTURE

1. Introduction

The NASA Orion space program represents the efforts of the United States to create a crewed spacecraft that can travel beyond Low Earth Orbit and then survive Earth re-entry at high return velocities. The Orion Multipurpose Crew Vehicle (MPCV) provides the environment for the crew and could eventually visit an asteroid or even venture further into deep space to destinations such as Mars.

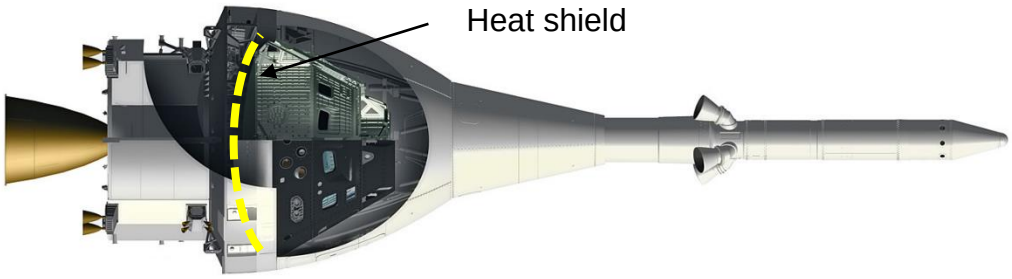

Figure 1: The heat shield carrier location (shown with a dashed line) within the MPCV vehicle stack.

The heat shield carrier (HSC) is a vital component of the Orion MPCV and is instrumental in protecting both the vehicle and its crew during re-entry and splashdown. It attaches to the underside of the crew module as shown in Figure 2:

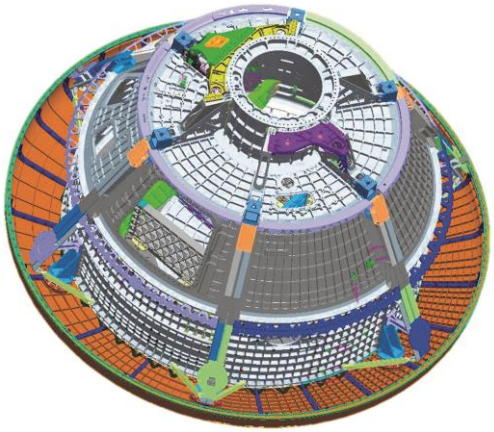

Figure 2: The heat shield carrier within the MPCV assembly.

The heat shield carrier must provide a sturdy foundation for the outer ablative layer, resist the effects of atmospheric re-entry, and bear the impact of a water landing without becoming an excessive mass burden on the Orion spacecraft. An Exploration Flight Test (EFT) 1 HSC developed and produced by Lockheed Martin Space Systems Company (LMSSC) came in above mass targets, prompting the NASA National Engineering Safety Center (NESC) to spinoff a team to investigate and design an alternate heat shield with the goal of a 25% reduction in

system mass over the baseline Titanium stringer-composite skin design. The team ultimately produced the design provided in Figure 3, which is comprised of an orthogrid stiffened dish supported by 15 truss segments, 18 stringers, and four retention and release (R&R) interface fittings.

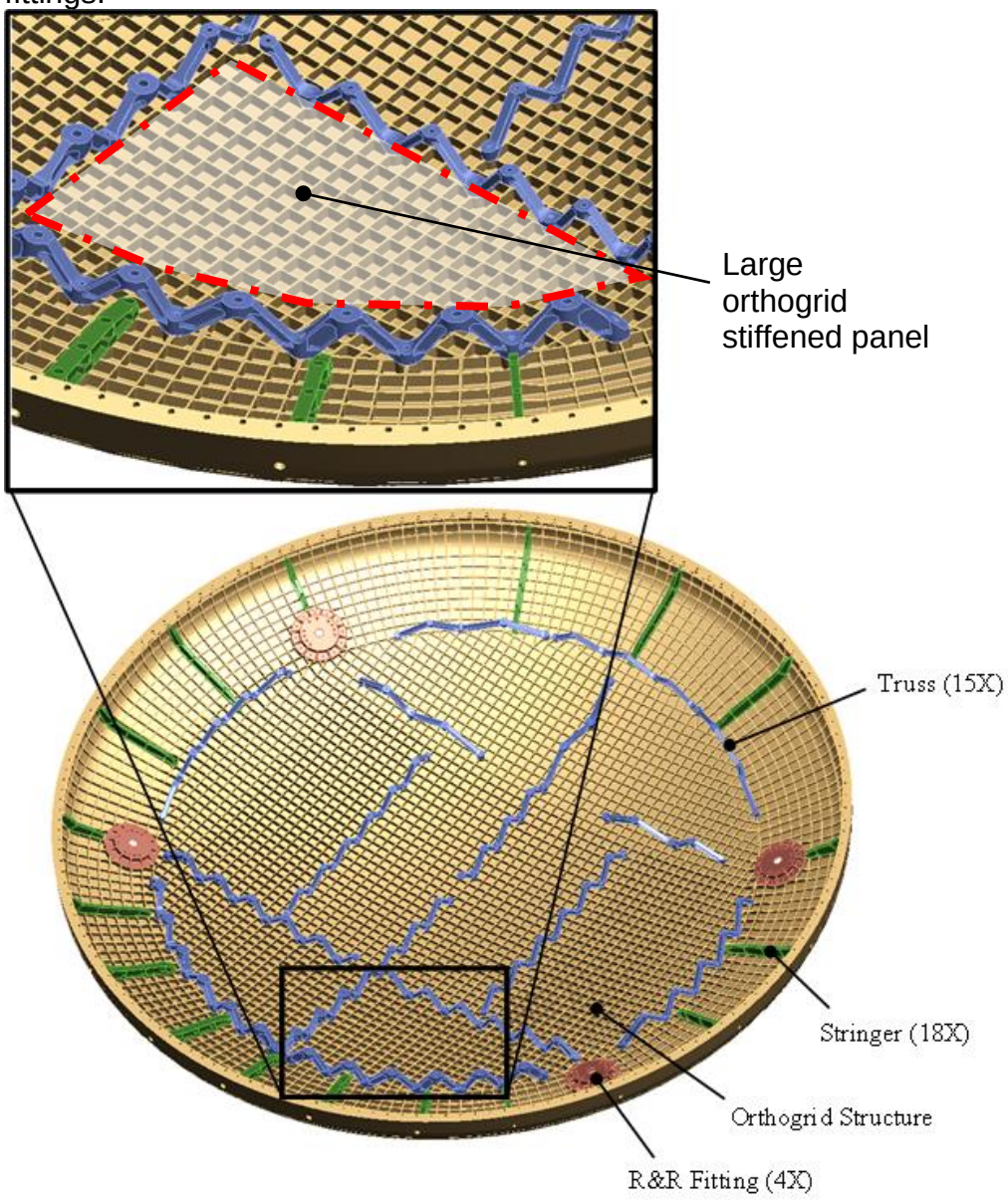

Figure 3: The final design for the NESC-proposed heat shield assembly.

This paper will focus on the innovative strategy to develop a design and analysis process to utilize multiple simulation codes to deliver the final lightweight design show in the previous figure.

2. Smeared Analysis Approach

Finite element models (FEMs) were used for trade studies and to substantiate the structural analysis. The commercially available HyperSizer analysis program was used to be able to quickly produce margins for a variety of concepts. HyperSizer is a software tool that works in concert with FEA solvers (such as Nastran) to evaluate panel-stiffening concepts and determine minimum weight structures. Smeared properties simulated the stiffnesses of open panels supported around their perimeter. These models were simpler, faster to iterate, and permitted the generation of a multitude of trade concepts in HyperSizer that could save mass. Figure 4 shows some concepts available in HyperSizer:

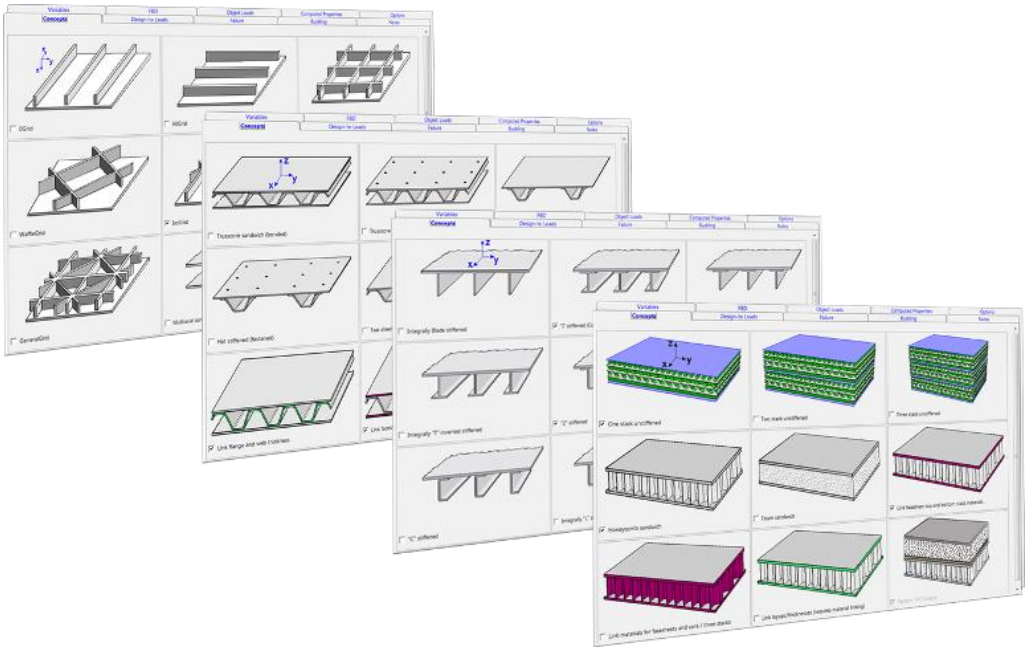

Figure 4: Candidate concepts available in HyperSizer

Some candidate examples include isogrid, hat stiffened panels, integrally blade stiffened panels, and sandwich panels. Figure 5 shows how each of these concepts gets turned into a stiffness formulation:

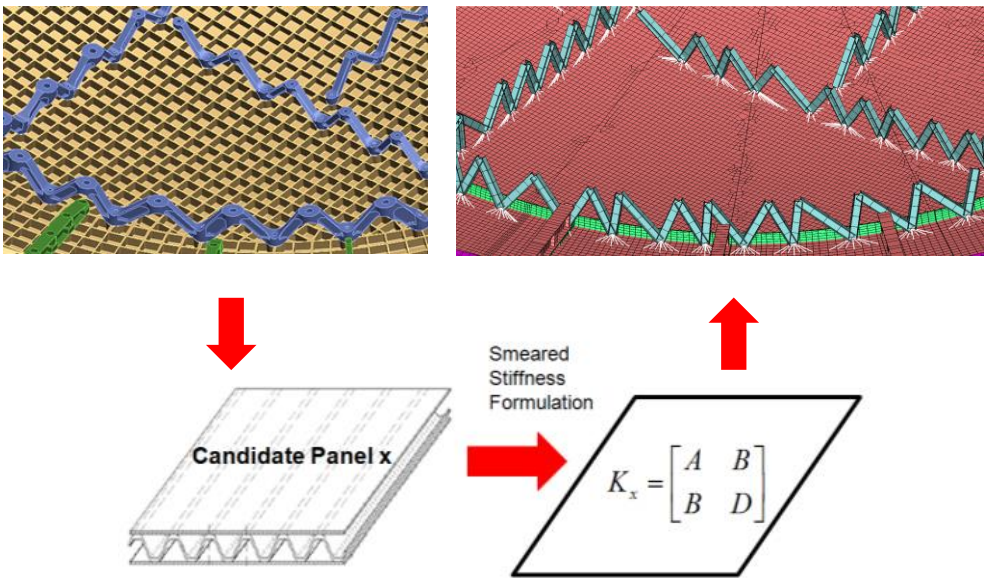

Figure 5: HyperSizer methodology for evaluating a multitude of structural concepts (Ref. HyperSizer).

A discrete set of potential panel stiffening architectures (such as orthogrid) are contained within a pool of candidate. After the smeared stiffness formulation is developed for a concept, it is sized for positive margins based on panel forces. A HyperSizer-internal process resolves FEA loading into object loads. This applies panel loads (extracted from FEA) to the structural features of a particular concept, such as the cross section of a hat stringer, in order to size them by local strength and stability-based failure modes with closed-form calculations. All candidate panels are then subjected to a quantitative comparison by weight (mass).

3. Dynamic Loading and Static Load Reduction

At the culmination of its mission, the MPCV returns to Earth and splashes down in the ocean as in the test shown in Figure 6:

Figure 6: Orion boilerplate drop-testing at NASA Langley (part of earlier program development).

Over the course of the splashdown event, the vehicle drops from a parachute-slowed speed of about 25 feet per second to zero. Forces exerted from water impact are by far the most significant form of loading the HSC must encounter. One of the greater challenges the team faced was how to assess trades, size designs, and generally analyze with tools developed for linear static loading environments.

A set of 125 landing load cases were developed by LMSSC that involved simulating impacts of MPCV at various angles and speeds relative to the water in LS-DYNA. LS-DYNA is an FEA solver that uses explicit time integration to study nonlinear transient dynamic events. The explicit transient code is commonly used for short-duration impact simulations of post-buckling behavior and is capable of simulating fluid-structure interactions. A water-impact model was run by the program to simulate the impact of the vehicle into a fluid volume (Figure 7).

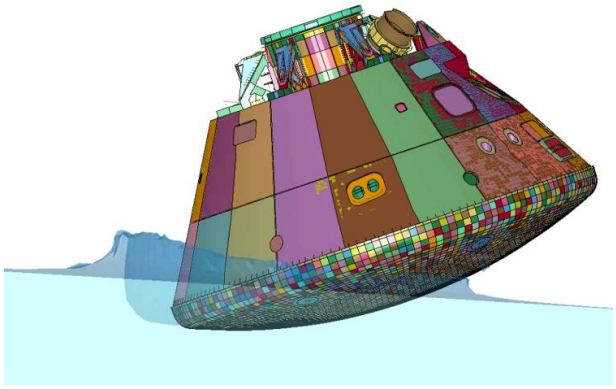

Figure 7: Simulation of the water landing with LS-DYNA.

Pressures from the fluid-structure interface were extracted from this simulation. The loading took the form of a pressure pulse that traversed the length of the HSC over a matter of about 100 ms. Figure 8 shows these pressures plotted at three moments in time:

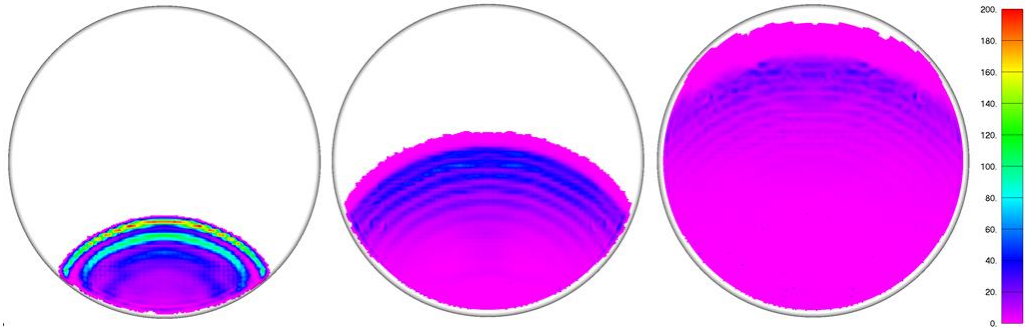

Figure 8: External pressure on the HSC skin from the LS-DYNA simulation. Areas of no color indicate null loading.

External pressures during LS-DYNA load cases were sampled at 1ms intervals. Combining the full durations of the impacts with all 125 load cases meant over 25,000 potential static load cases to choose from. This is a prohibitive amount of load cases to consider, so it was concluded that a “representative set” of static loads would be used instead. These would be determined by calculating the load case and time step combination that produced the largest sum of pressures over all elements over a portion of the HSC skin or “bay”. This method was only valid if the skin element sizes were consistent; each skin element was in fact close in size. The HSC skin was first divided into 7 arbitrary but logical bays.

Figure 9 demonstrates the pressure wave peaking in successive bays from the windward (side of first impact) to leeward sides.

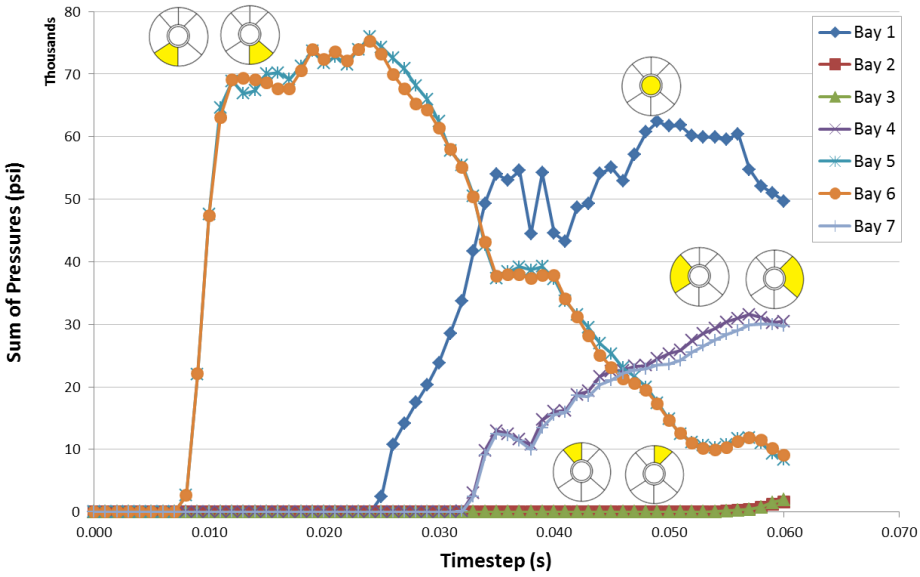

Figure 9: The sum of pressures for each bay over all time steps for a particular load case. A diagram highlights the bay corresponding to each curve.

The pressure over a single bay is plotted for all load cases.

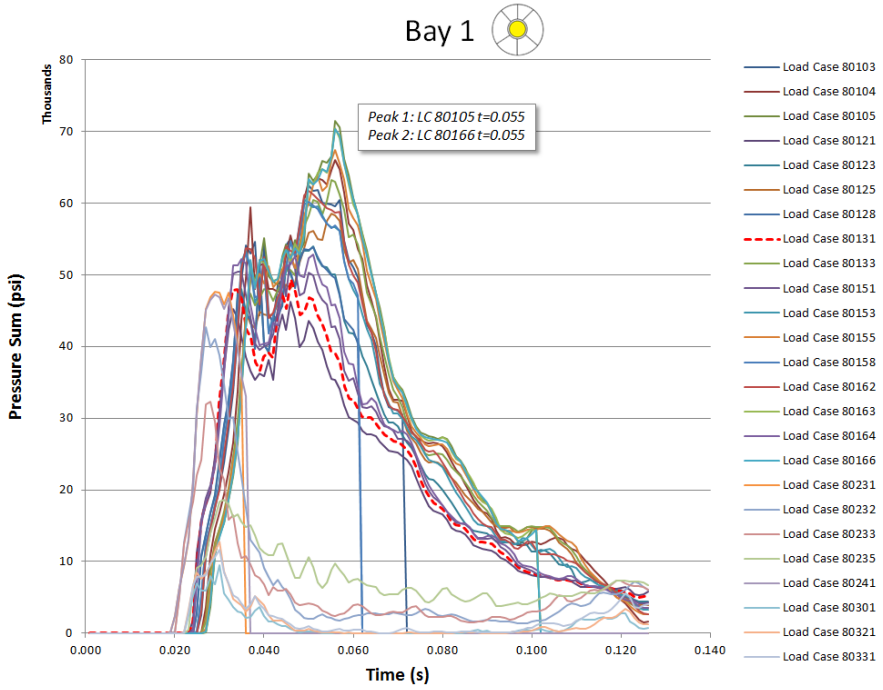

Figure 10: Pressure summed over all bay one elements for all dynamic load cases.

As shown in Figure 10, two load cases (80105 and 80166) are clearly more severe than all others at the 55 ms mark. Significantly more bays

(46) were considered in the final round of load reduction. This load reduction method culminated in 70 unique static landing load cases. The envelope of these load cases (for demonstration only, not sizing) is plotted in Figure 11:

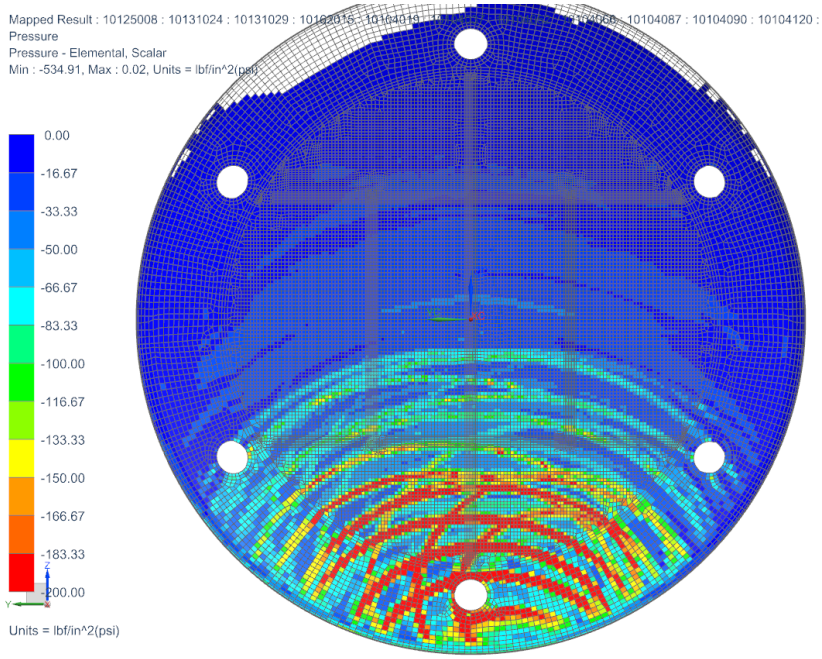

Figure 11: Enveloped landing pressure from 70 static load cases.

Some off-center impacts can be seen as well. The peak pressure from the traveling pulse reaches over 500 psi, but that level of loading only spans a few elements at most, and only for a very short period of time. As more of the HSC outer surface becomes wetted and the vehicle decelerates, the pressure pulse drops in magnitude before reaching the leeward side.

Re-entry loads had the form of a mostly uniform pressure distribution on the outer surface and were much less severe than landing (~10-15 psi). Peak external pressure on the HSC from aerodynamic forces were an order of magnitude less than landing pressures and came from an off-nominal lunar return case. Crew module internal pressure was combined with a single critical re-entry case. This load case was considered static as the peak loading is relatively constant over a matter of seconds.

4. Trade Study

At the onset of the project, the program implemented a design change to the angle at which the MPCV “slices” through the water surface at landing to reduce impact decelerations. This adjustment stems from a

change in the hang angle of the MPCV as it is suspended by a parachute prior to splashdown. The original design would therefore see big mass changes while it was carried through the trade analysis. The project was not limited in scope to introducing new architectures; should the composite skin/ Titanium stringer design show the most potential, it could be selected moving forward into the next stage for refining the final design. Initial new candidate designs were indeed just evolutionary modifications to the original design. Analyses were carried out on recent FEMs received from the inline heat shield development team using HyperSizer and Nastran to support the trade study. The stages of the trade study are shown in Figure 12.

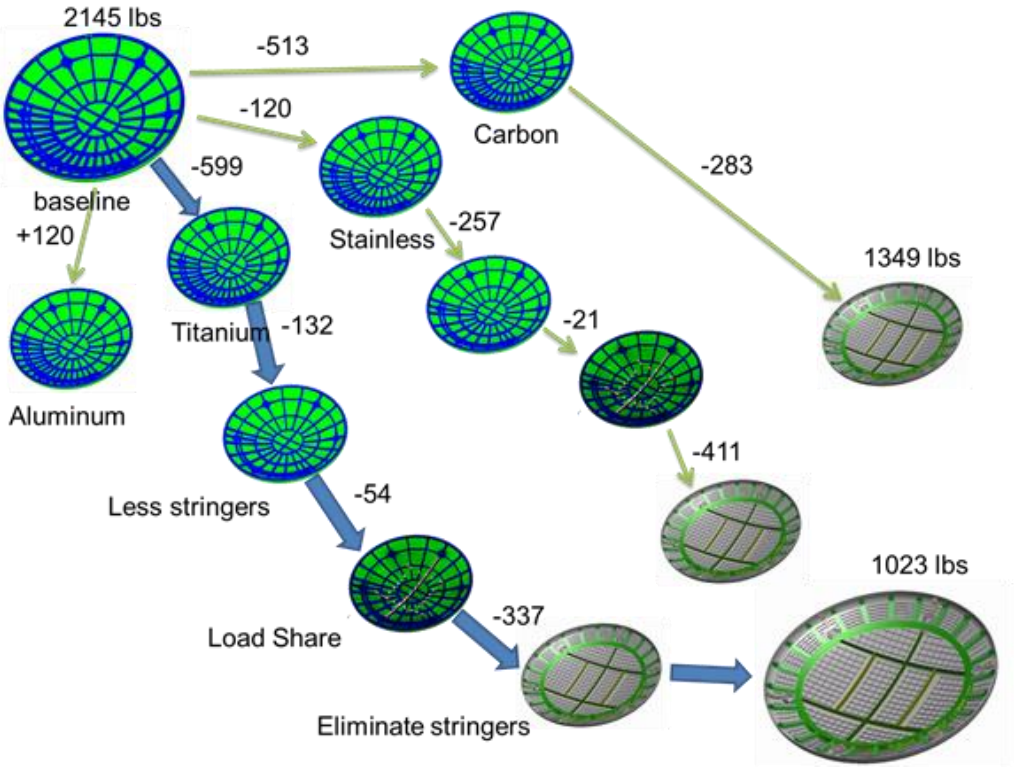

Figure 12: Trade study concepts and their effects on structural mass.

The first stage traded materials on the original “wagon wheel” skin and stringer design, adding into consideration three metallics on top of the carbon composite used for the original skin. Titanium and composite materials demonstrated the greatest potential mass savings, but Stainless Steel and Titanium-based designs were carried through. The steel wasn’t optimum due to a lower specific stiffness (stiffness/density)

than titanium, but it was still carried through[1]. Aluminum didn't have the most favorable high-temperature strength or specific stiffness properties and showed not to be competitive for mass. The carbon design did not save as much mass since it required very thick laminate regions to balance high out of plane pressure loading with relatively weak transverse properties. Substantial mass savings were predicted by eliminating unnecessary stringers, as their placement was previously optimized for the old hang angle. New models with an increasing number of deleted stringers were analysed in HyperSizer. The mass impact is shown in Figure 13:

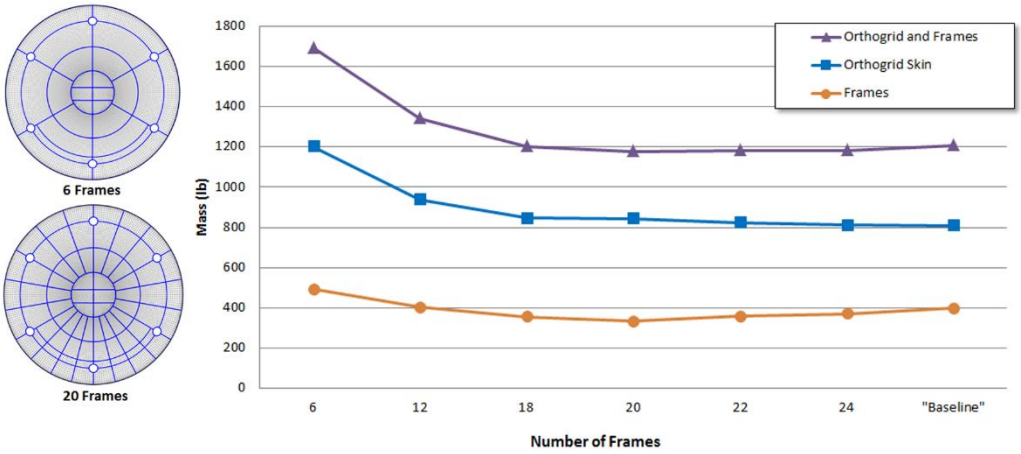

Figure 13: Stringer (frame) number mass impact study.

The next trade brought an interface change to the configuration. Instead of maintaining the original interfaces, the center acreage of the carrier structure was tied to the pressure vessel in an H-pattern to match the stiff backbone structure footprint of the MPCV as seen in Figure 14:

[1] The Stainless Steel design was carried through since it offered the best manufacturability and CTE matching to the Avcoat bonded to the skin, a separate issue outside the scope of this paper. The primary driver of the project was structural system mass.

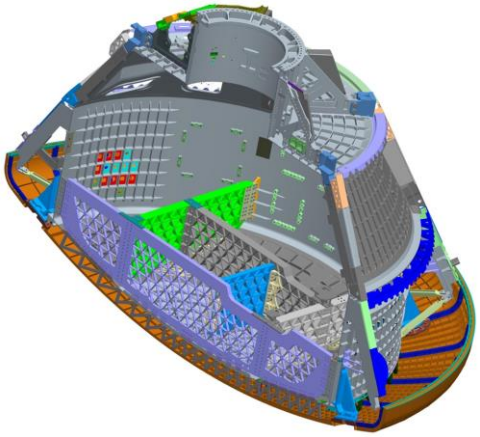

Figure 14: Cross section of the MPCV showing the backbone backing structure integral to the design of the load sharing truss design.

Although only a small benefit was initially seen, a subsequent design configuration change to orthogrid in order to take advantage of the load sharing concept afforded a substantial mass savings. This last design was further refined using the methods discussed later in this paper to arrive at the estimated mass number of 1023 lb, a mass savings of over 1,500 lbs.

5. Finite Element Models and Static Analysis

The trade study (discussed in the next section) demonstrated that orthogrid could deliver the greatest mass savings to the heat shield. An example of orthogrid is provided in Figure 15:

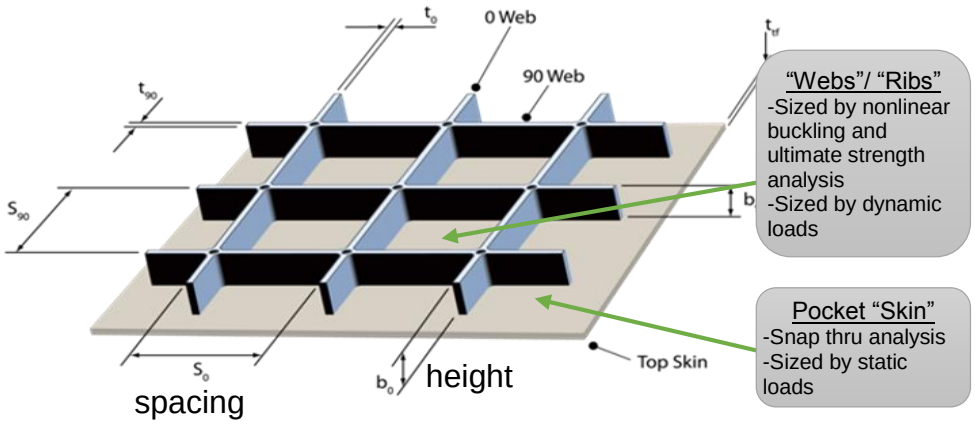

Figure 15: Orthogrid features and terminology as used in this paper.

The orthogrid sizing in HyperSizer began with a smeared model analysis procedure outlined in Figure 16:

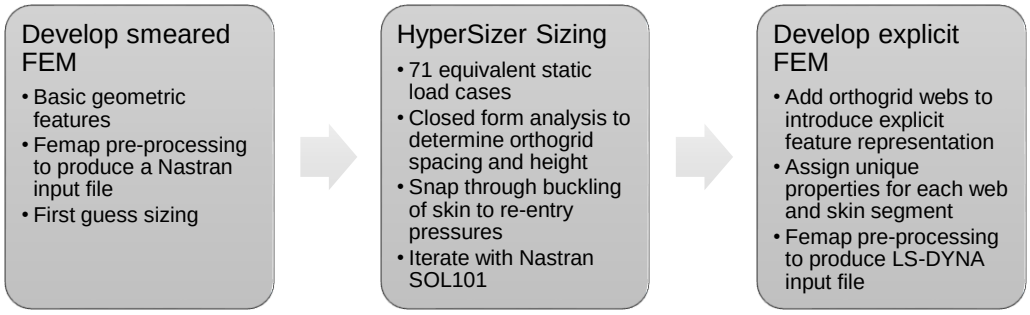

Figure 16: Smeared HSC FEM sizing process.

Traditional modeling practices use “loads” and “stress” FEMs, with the former suitable for initial sizing and the latter typically serving to verify prior conclusions about model behaviour. Analogous to the standard two-model system, two independent FEM types were developed and maintained for this project. The first FEM type used in preliminary sizing and trade studies utilized smeared properties. A smeared heat shield FEM is shown in Figure 17.

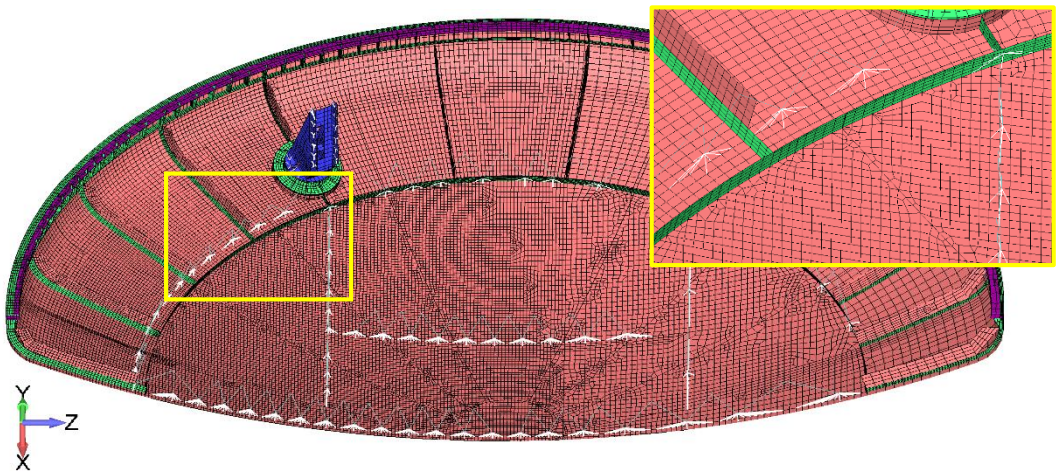

Figure 17: Smeared heat shield carrier FEM used for global orthogrid sizing (right side shown for clarity).

Panels in a smeared FEM are modeled only with 2D skin elements. Such FEMs were used to evaluate panel buckling and size for orthogrid spacing and heights for the purposes of trade studies. This FEM type has only basic architectural features, such as an outer surface and a connections to existing vehicle interfaces. No orthogrid stiffeners existed in this type of model. Approximately 87k elements comprised the smeared FEM.

All 71 static load cases were analyzed with the smeared model in HyperSizer. Material properties at "hot" post re-entry temperatures were only used with the landing cases. HyperSizer then produced rough sizing parameters, such as web spacing and height, from which an explicit FEM was constructed. The explicit FEM type was a detailed representation of geometric features of the chosen concept. This FEM (Figure 18) enabled final detailed analysis.

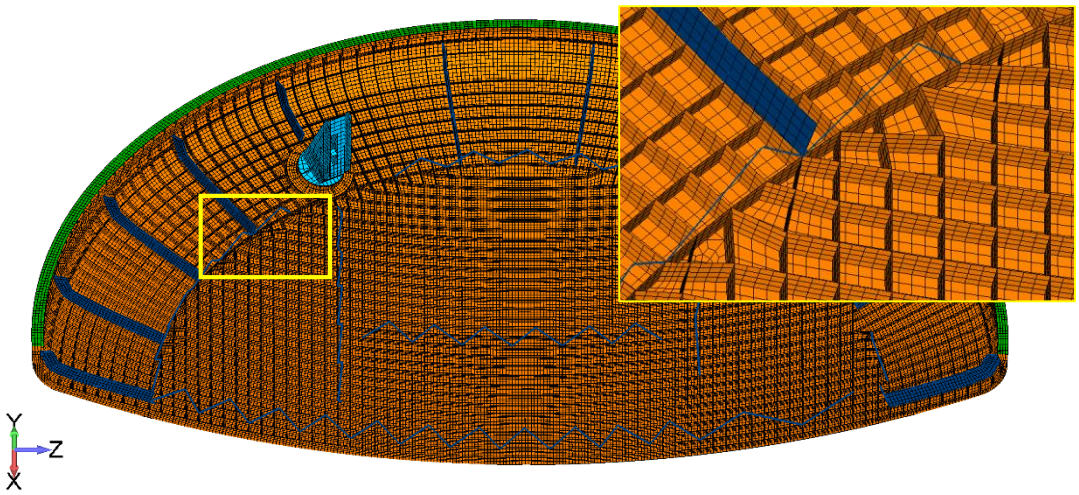

Figure 18: Explicit heat shield carrier FEM used for local orthogrid dimensional sizing (right side only). Colors indicate element material type. Inset image included for clarity.

Since this type of FEM explicitly modeled the orthogrid web and skins elements, it could be used to assess local strength and stability. Each pocket contains three or four walls, referred to as "webs", and a skin.

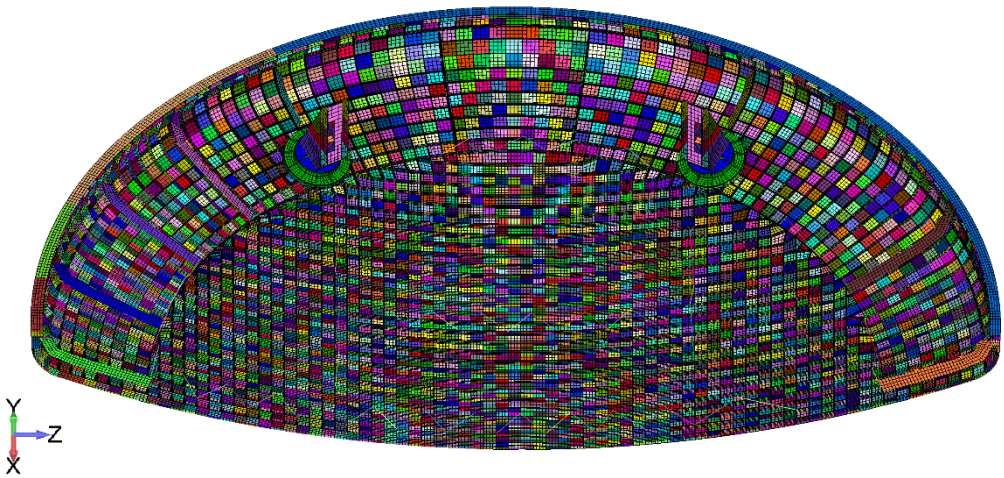

Figure 19: Explicit heat shield carrier FEM used for local orthogrid dimensional sizing (right side only). Colors indicate unique property region.

Each wall was meshed with four elements through the height. This would enable nonlinear sizing to size based on in-plane moments extracted from FEA results. Approximately 240k elements comprised the explicit FEM. Another view of structural components in the explicit FEM is provided in Figure 20:

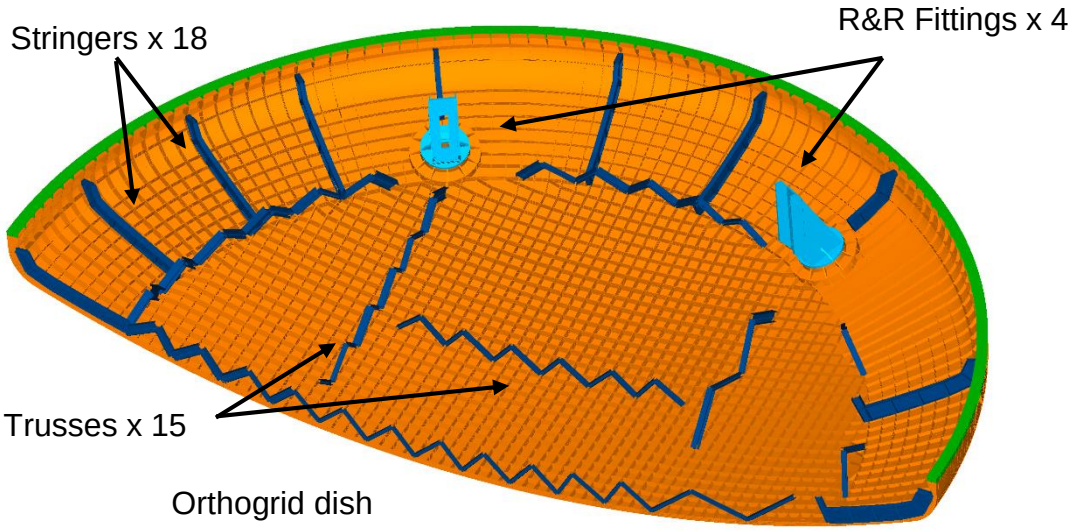

Figure 20: Explicit heat shield carrier FEM with major structural features labeled. Right side shown.

The original composite skin/ Titanium stringer HSC interfaces with the rest of the vehicle in three locations, with the NESC design adding a fourth. A lower fidelity vehicle FEM was mated to the HSC to provide appropriate load paths to the vehicle CG in order to achieve accurate distribution of reactions at the HSC-MPCV interface.

The smeared and discrete FEMs were created in the Femap pre-processor in Nastran format from CAD geometry. A significant investment of effort was made into the organization of the complicated models. Approximately 5,000 skin properties and 10,000 web properties were needed for the orthogrid mesh alone. Although this permitted detailed sizing of local regions for maximum tailoring of gage thicknesses, it initially proved difficult to manage such tasks as updating each property after a round of sizing. For this reason, some advanced features of Femap such as API programming were used to reduce the time to complete repetitive tasks such as implementing design changes as influenced by the optimization process.

The HSC orthogrid pocket skins have a doubly curved shell (spherical shape) assumed simply supported by orthogrid webs and loaded by external pressure against the convex face. The skins under re-entry loads are not permitted to buckle/snap-through. Deforming the skin,

even elastically, puts the Avcoat at risk during this mission phase. Landing loads are treated differently, since by this point the Avcoat layer is structurally expendable. This distinction is critical to mass savings as the skin is permitted to buckle inward from the more substantial landing loads. Note the difference in pressure magnitudes in Figure 21.

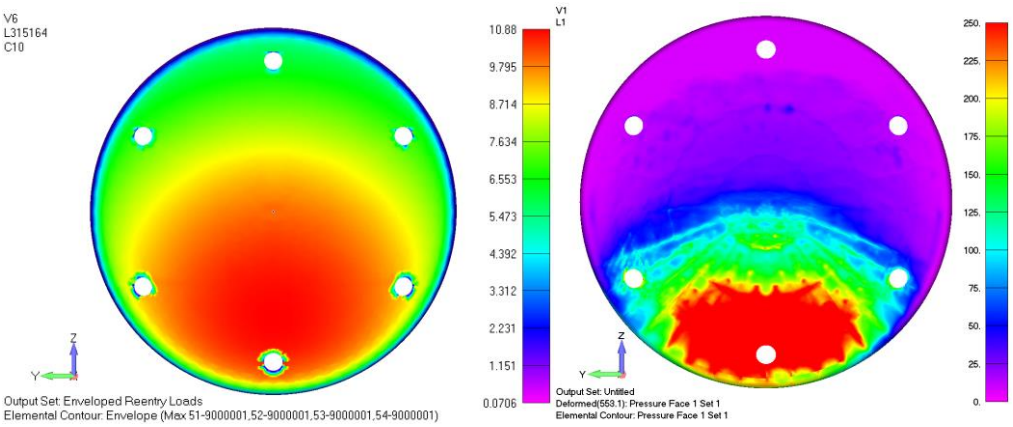

Figure 21: Worst case re-entry pressures (left) and enveloped landing pressures (right).

Limit re-entry pressure peak at about 11 psi, while landing loads peak well over 250 psi. By permitting buckling of the skin (but not the panel as a whole), the skin (Figure 22) is allowed to react the pressure in membrane, much like a balloon holds air with in plane stiffness. This allowed the thickness-controlled bending stiffness to size down. Nonlinear dynamic predictions in LS-DYNA suggested the pocket skins could easy resist landing pressures in membrane without failure. This left the sizing of orthogrid skin to re-entry pressures. Calculations were made on the re-entry pressure required to buckle in the bare skin without Avcoat. No stiffness from the Avcoat layer is considered (it is only represented as mass in the global model). Limited literature exists for theoretical predictions of the expected snap-through failure mode of this particular shape. Isolated local pocket skin FEA models in conjunction with similar closed form solutions determined the dependency of snap through on external pressures.

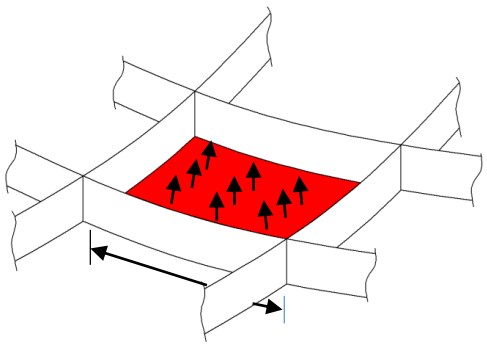

Figure 22: Local analysis of orthogrid skin (red) limited to individual pockets.

FEMs of various edge distances and skin thicknesses were analyzed with Nastran to determine snap through tendencies. The characteristic behavior of snap through is shown in Figure 23.

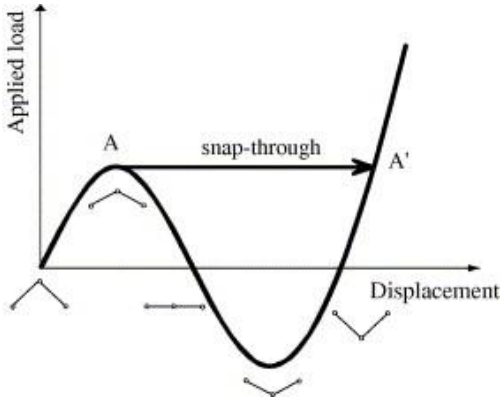

Figure 23: Load vs. displacement snap-through behavior.

Applied load increases to a point A. The skin has reacted the pressure in compression and bending by this point. Beyond the critical point A, the load drops as the panel reaches its alternatively stable mirrored form. After the skin “pops” or snaps” through, it may continue to react an increasing amount of load, but no longer in compression since the shape has inverted. There is more capability in the skin because it is being reacted by a tensile load and there are no more instabilities. A closed form solution for the critical pressure at A after which snap-through is initiated is taken from Roark. Consider the curved panel under uniform radial pressure, q with pinned infinite edges A and B:

$$q' = \frac{Et^3\left(\frac{\pi^2}{\alpha^2} - 1\right)}{12r^3(1-v^2)} \qquad \alpha = \frac{AB}{2r} \tag{1}$$

Where q' is pressure at which buckling occurs, AB = arc length, and r is radius of curvature. Snap-through behavior was not immediately obvious from the displacement plots. The elemental loading is instead used to gauge the pressure at the onset of snap-through. The pressure at which the Nastran calculated elemental membrane forces reach a minimum compressive value matched well with the closed form solution for Roark buckling for every Nastran model analyzed. One example is provided in Figure 24.

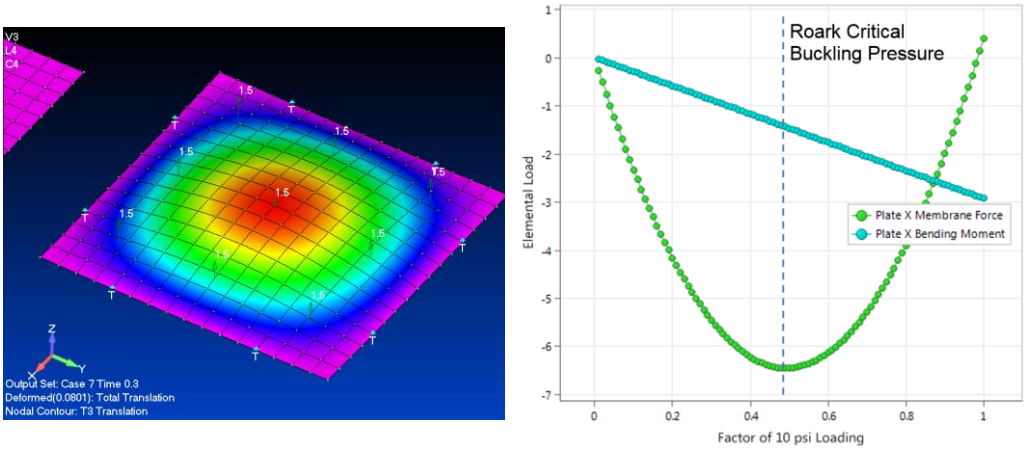

Figure 24: One of the FEMs used to investigate snap-through behaviour (left) and a plot showing the critical buckling pressure as predicted by Roark and validated by Nastran (right).

For sizing, the Roark formula was used with a fixed boundary factor to size orthogrid pockets from ultimate re-entry pressures. Fixed supports by the skin-web interface were assumed since the snap-through calculations indicated the orthogrid would require short edge distances with ¼ in fillets as set by manufacturing requirements. Skin margins for ultimate strength were also checked with the von Mises-Hill criterion but were generally not a driver.

6. Comparison of LS-DYNA and Nastran Solutions

An aggressive approach to the early analysis was to not size local members for buckling due to the near instantaneous application of pressures from the water impact. This approach was validated by simulations for the forward facing (windward) side of the HSC, but failed

to be appropriate for the leeward side, which bears landing pressures for a non-trivial amount of time as the water impulse slows.

LS-DYNA results on an early design indicated buckling below limit loading, prompting a nonlinear static comparison with Nastran. External pressures on the HSC placed the orthogrid free edges in compression towards perimeters of the panels, and buckling occurred. The results were still valuable, as they demonstrated nearly identical behavior of the interior orthogrid-supported panels between the solution codes, which included local web buckling initiated along the panel perimeters.

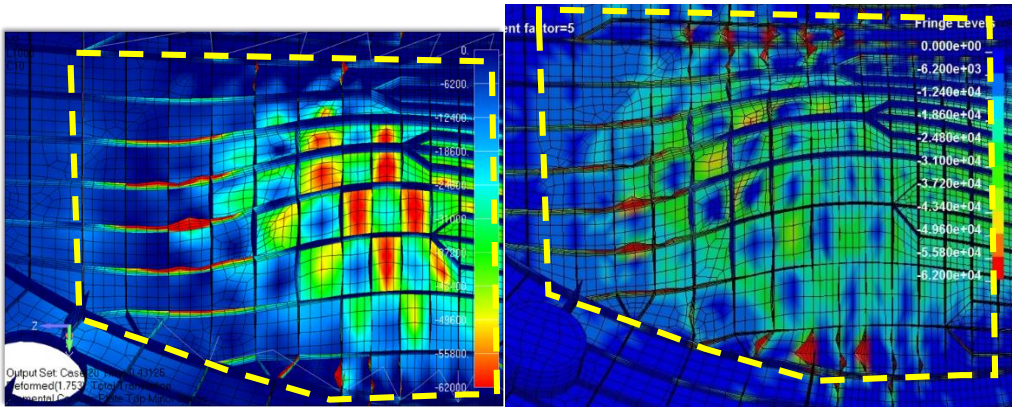

Figure 25: Nastran SOL106 (left) and LS-DYNA explicit (right) solutions of one of the early orthogrid designs. Panel perimeters are outlined.

Such a comparison was also important to verify such congruency between Nastran and LS-DYNA solutions, as the initial sizing would be performed using Nastran static results and final sizing with LS-DYNA dynamic results.

7. Dynamic Simulations and Nonlinear Orthogrid Sizing Process

Dynamic simulations were carried out with LS-DYNA using the explicit model. The explicit model was required in order to accurately assess the behaviour of the stiffening features. With this additional information, further sizing of the orthogrid could be completed. This sizing would entail predictions of localized yielding through nonlinear assessments of stiffness, strength, and stability in the explicit FEM. This process is outlined in the following diagram in Figure 26:

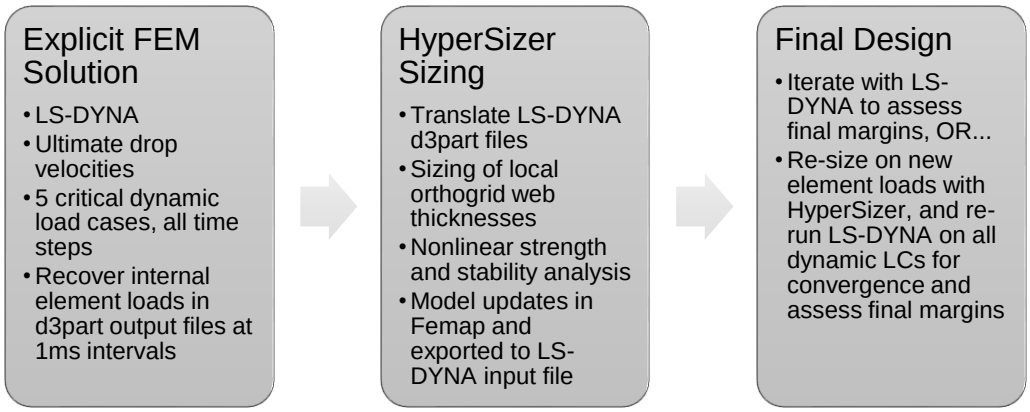

Figure 26: Explicit HSC FEM sizing process.

The first explicit model was generated with dimensional parameters from the static analysis in Femap and translated into LS-DYNA input file format. Five critical dynamic load cases were simulated at ultimate drop velocities, and elemental shell loading was recovered at 1ms intervals. The recovered output from all 100+ time steps of each of these load cases were translated into Nastran OP2 binary format and subsequently imported into HyperSizer for local nonlinear sizing of orthogrid web thicknesses.

Orthogrid buckling is generally critical as the IML free edges are in compression under landing loads. A Nastran nonlinear transient analysis demonstrated the buckling behavior of a web is shown in Figure 27.

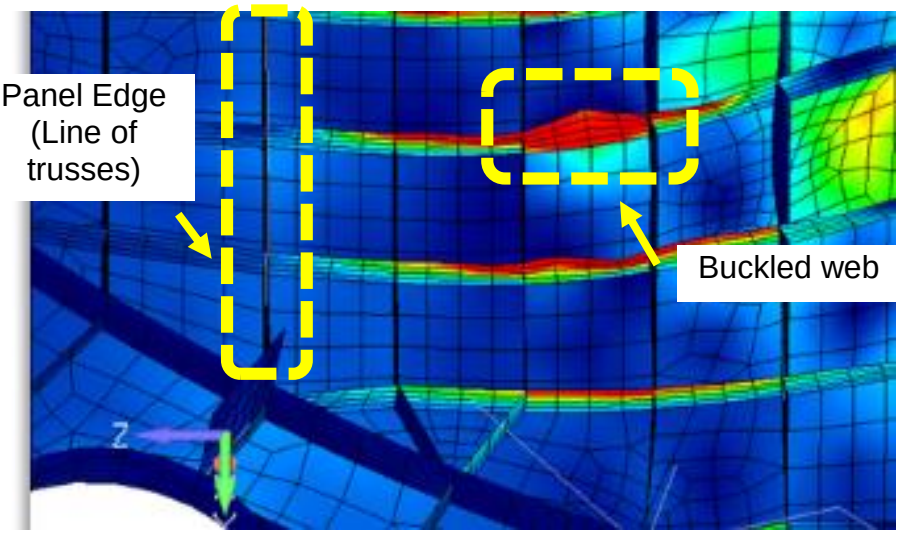

Figure 27: An orthogrid web that has buckled.

A procedure was developed to use raw dynamic model output to deduce axial load and in plane bending moment that prompted each web to buckle. A diagram of these loads is shown in Figure 28:

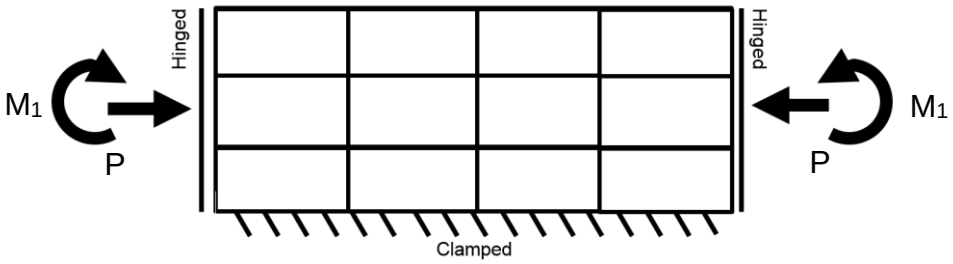

Figure 28: An orthogrid web subjected to in plane axial and bending loads.

These two values determine the neutral axis and outer fiber stress for the group of elements belonging to each web member, and size the web based on the buckling allowable:

$$F_{b,cr} = K_b \eta_c E \left(\frac{t}{b}\right)^2 \quad (2)$$

$F_{b,cr}$ is the critical buckling stress for a plate under normal and bending loads, K_b is the plate buckling coefficient (a function of the ratio P/M), and η_c is the is the plasticity reduction factor. The critical buckling stress that factors in bending can be 135% higher than consideration of compression across the entire web alone. This highlights the additional strength that can be reflected in sizing to lower structural mass. This operation is performed to size the majority of orthogrid web members. The balance is sized by ultimate strength, a function of the interaction between ultimate plastic bending moment and axial load. Figure 29 shows the loading for the rectangular webs.

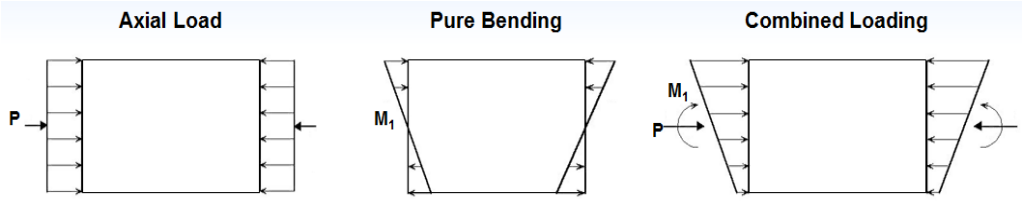

Figure 29: The equivalent beam loads extracted from FEA.

The component axial (P) and bending (M_1) loads are extracted from LS-DYNA results. Axial load ratio is calculated:

$$R_1 = \frac{P}{P_u} \quad (3)$$

Where ultimate axial force is calculated using F_{tu} or F_{cy} depending on the sign of the force. Bending load ratio is calculated:

$$R_2 = \frac{M_1}{M_r} \tag{4}$$

Where the resisting moment M_r has contributions of a plastic bending moment M_p for webs in tension and compression and ultimate bending moment M_u only for those in tension. The moment M_p is the maximum moment the cross section can resist before becoming fully plastic, and M_u is the additional moment the cross section can resist before rupturing at ultimate strength.

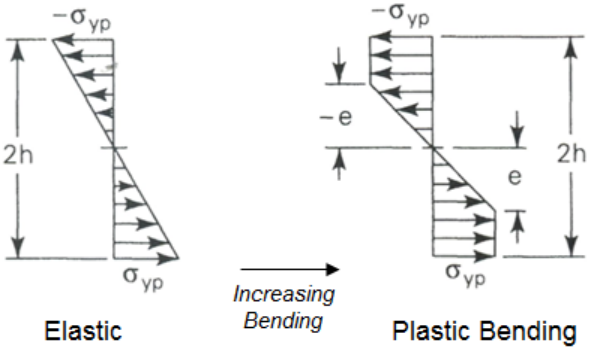

Figure 30: Stress distribution assumptions in rectangular webs after yielding.

Plastic bending analysis assumptions for the rectangular webs assumed a trapezoidal stress distribution after yielding as seen in Figure 30; this is in line with elastic-perfectly plastic behavior assumptions. The ratios are combined with the following interaction equation:

$$R_1^2 + R_2 = 1 \tag{5}$$

This ultimate strength margin writing process takes full advantage of material plasticity where possible. Since the webs are the dominant panel stiffening members, they contribute a significant portion of mass to the structure and are therefore the most important to size efficiently.

Localized sizing of the explicit model with dynamic internal element loads required that no buckling to occur. Should the load in the orthogrid webs redistribute (away from a local member) due to local buckling, the sizing process would cease to be effective as any sizing would erroneously drive the local thicknesses to zero. It was therefore important to preclude buckling by sizing slightly conservatively with the most severe dynamic loads first.

8. Drop Testing

Many of the analysis challenges focused on the strength and stability analysis of orthogrid. In order to validate the methods developed for sizing, testing was completed with a drop tower on a 20” test article shown in Figure 31. This test article had uniform web and skin thicknesses with a thick support ring around the perimeter.

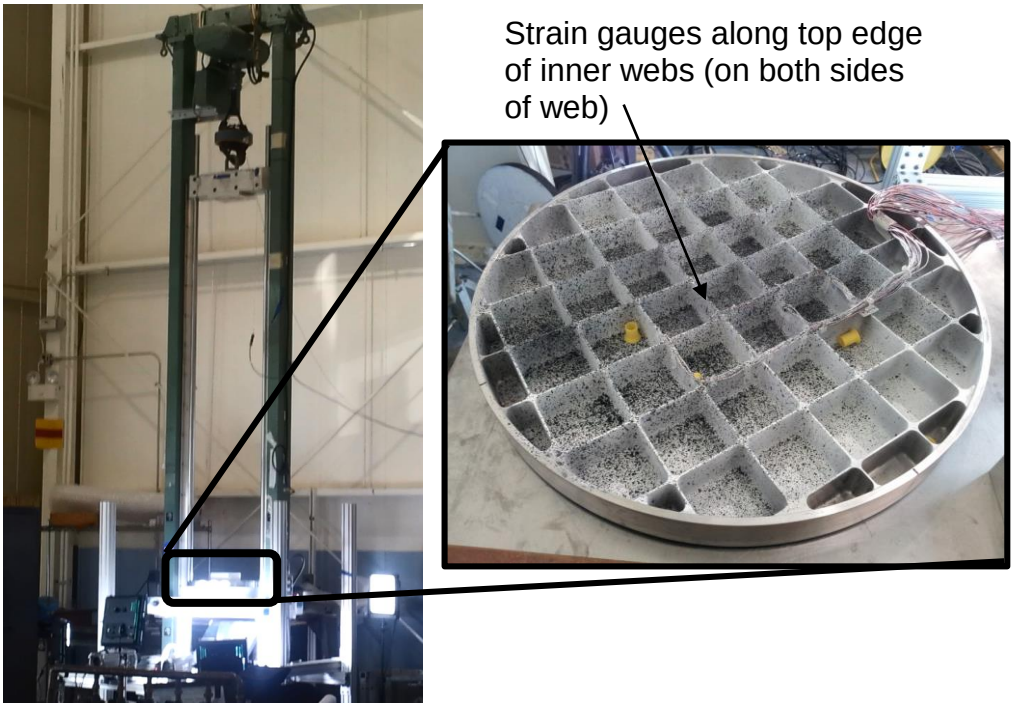

Figure 31: The subscale orthogrid test article (shown with a speckle pattern and embedded strain gauges) and the drop tower.

The test article was outfit with strain gauges along the height direction of the web member. The drop mass of 100 lb was released from up to 8.3 ft and directly impacted a foam block resting on the test article. Different foam types were used to tune the decelerations and thus force imparted on the test article. The test article was placed in a drop tower in one of two configurations, differentiated by whether or not the impact put the free edges in tension or compression.

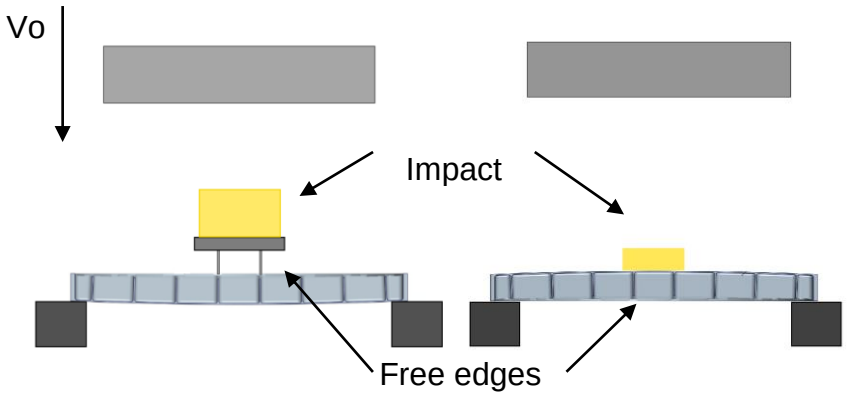

Figure 32: Diagram and test configuration FEM of the inverted (left) and upright (right) drop tests.

With the test article oriented in the upright position, the orthogrid free edges are placed in tension when the structure reacts the impact of the drop mass. In the so called “compression” or “inverted” test, the load is introduced into the orthogrid on the side of the webs and not the skin. To accommodate such a drop configuration, an impact plate is bolted to the intersections of the four inner webs. Half-sine wave external pressure pulses were simulated as load input for both tests. The models are shown in Figure 33:

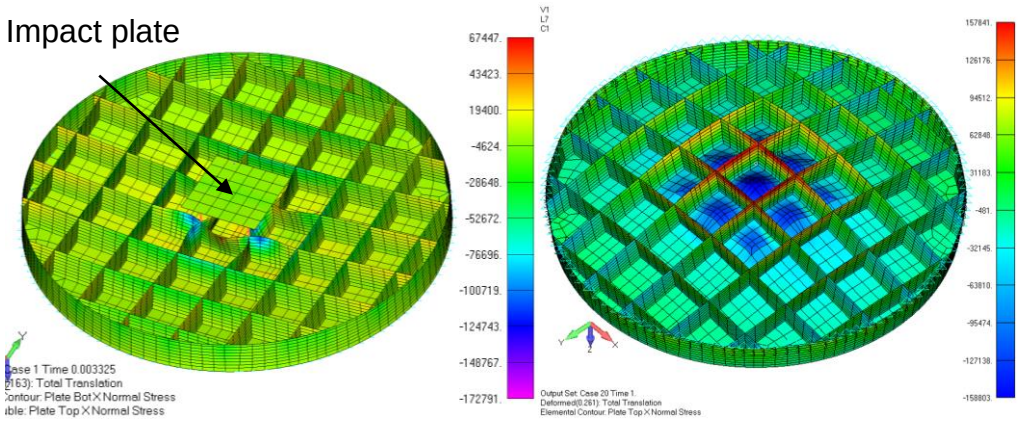

Figure 33: Analysis FEMs used for inverted (left) and upright (right) test predictions.

The Nastran nonlinear transient solution SOL129 was used to predict the onset of plastic behaviour while in an upright position and (separately) the onset of web buckling with the article in the inverted position. A bi-linear elastic-perfectly plastic material definition was used for Titanium. The large displacement (LGDISP) Nastran parameter was used to account for geometric nonlinear effects.

The strain responses from the last upright test and simulation are in Figure 34.

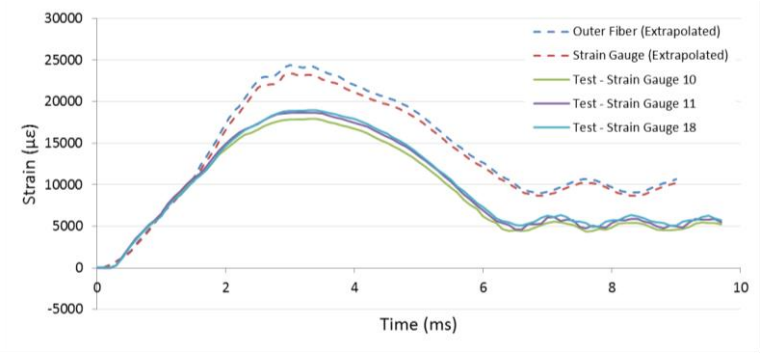

Figure 34: Strain gage response versus time for Nastran and test.

Two curves from the Nastran FEM results are plotted. One is the strain at the outer fiber and the other is at the strain gage location along the depth of the web. Both values are extrapolated from a best fit curve of strain versus web height since the Nastran results are produced at the element centroids. The strain did not align with the test results. Peak Nastran-predicted strains are about 25% higher with twice the remaining permanent set. The difference was discovered to be from the dynamic yield strength. The nonlinear material properties stem from tensile tests that loaded a specimen at a particular rate within the capability of the testing machine. The peak strain rate from the tensile tests was 1.41 in/in/sec, though the strain rates from test were closer to 12 in/in/sec. The analytical yield strength of the material was therefore adjusted upwards by 31% based on the strain rates during the test and use of Cowper-Symonds empirical material parameter. The nonlinear transient solution was repeated; the results are shown in Figure 35.

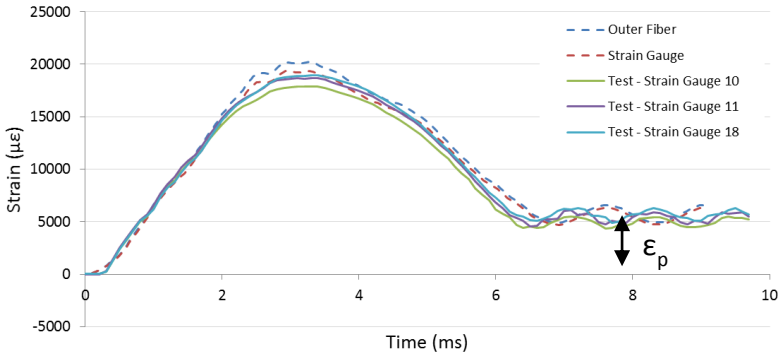

Figure 35: Strain gage response from Nastran and test using a strain rate corrected yield stress.

The response correlates much better with the yield strength corrected for strain rate. Both peak strain and plastic strain were predicted with good accuracy. About 0.5% plastic strain is left after the impact. The comparison with LS-DYNA results were similarly succesful:

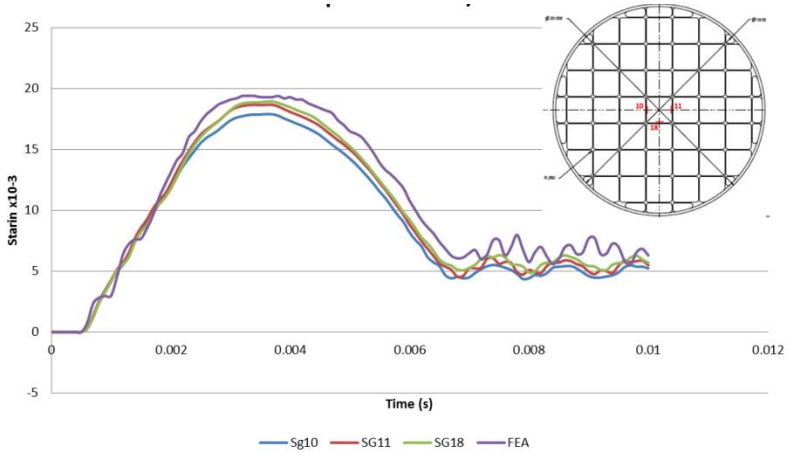

Figure 36: Strain gage response from LS-DYNA and test using a strain rate corrected yield stress.

These results in turn exposes a built-in conservatism with the analysis. During the HSC sizing, yield strengths were not adjusted for strain rate.

The inverted test took place after the tensile test. Pre-test predictions showed that the inner-most webs of the test article would buckle after an introduction of a 9 kip peak load over an 8 ms pulse.

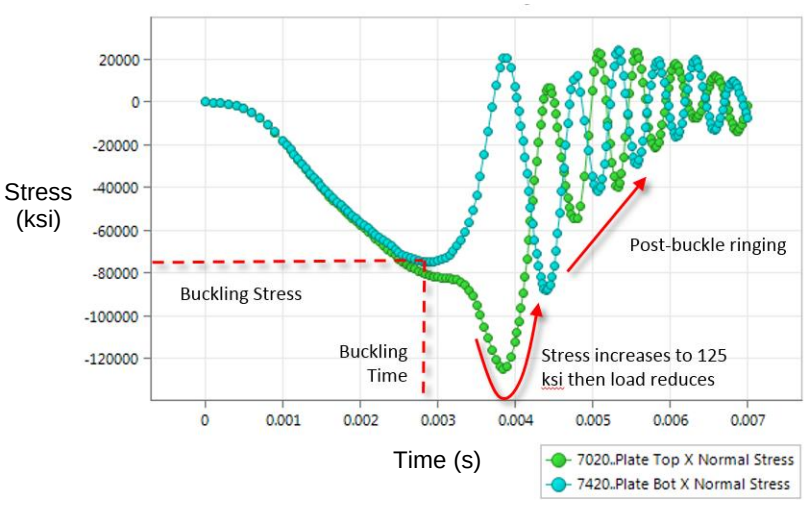

Figure 37: Plate element top and bottom stresses in the outer fiber element.

The Margin of Safety plotted versus time as calculated from Nastran elemental loading and equations (3), (4) and (5) is shown in Figure 38

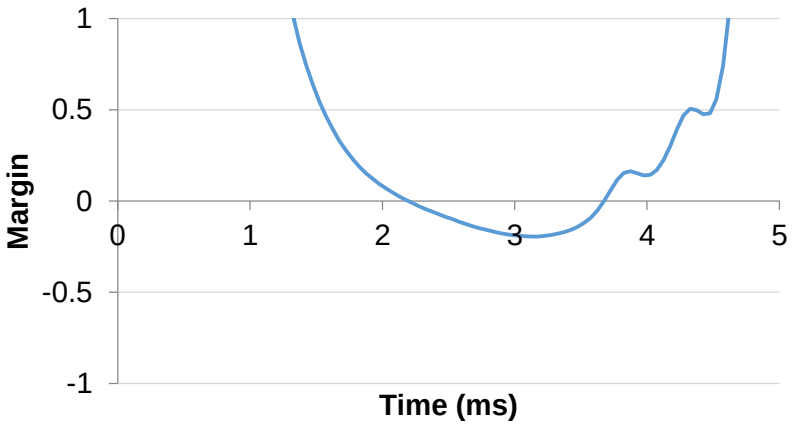

Figure 38: Inner web buckling Margin of Safety (no Factors of Safety applied) against buckling.

The margin predicts buckling to occurs slightly after 2.3 ms. The drop test was completed with a peak loading of 7.7 kips and pulse duration of 7.4 ms. The response of back to back strain gauges installed on both side of the inner-most web is plotted.

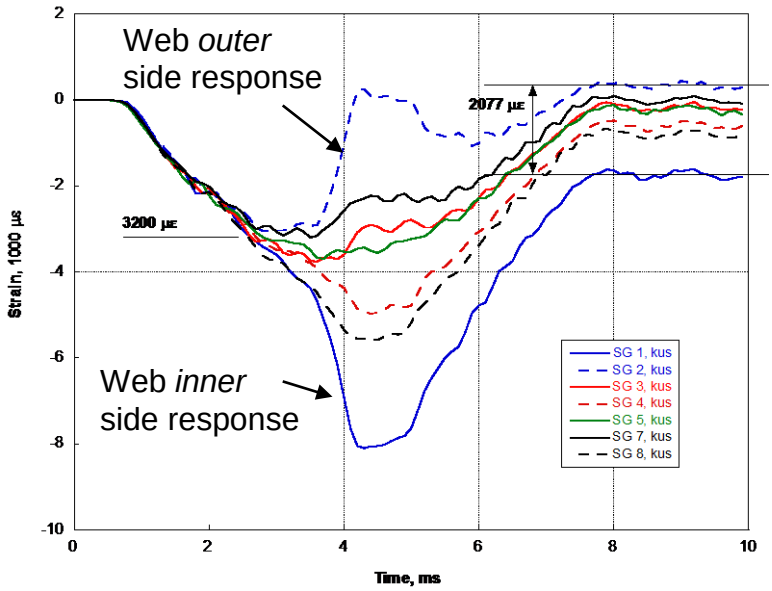

Figure 39: Outer fiber (free edge) strain response of the instrumented inner web during the inverted drop test.

Web buckling is initiated around the 2.5 ms mark, as evidenced by the diverging strain gauge responses demonstrating a marked increase in bending as a result of buckling. Figure 40 is a photograph of the test article before and after the inverted test.

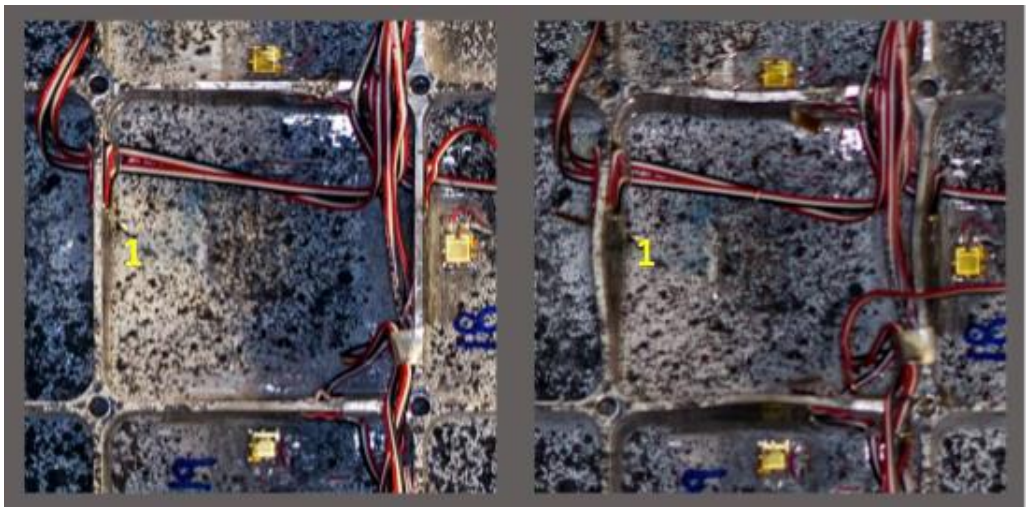

Figure 40: The inner-most webs before (left) and after (right) the inverted drop test.

The first test left stress in the center webs; this could have in turn prompted buckling at a lower level of impact force. The test successfully demonstrated the damage tolerance nature of orthogrid. The redundant stiffening members were more than able to contain the impact load and prevented catastrophic buckling of the test article.

9. Conclusion

Iterating designs with Hypersizer and LS-DYNA took advantage of the inherent damage tolerance of the orthogrid concept by permitting loads in certain components to redistribute in a specific, non-detrimental manner. This approach effectively used material plasticity to save mass. The final orthogrid-based design also overcame initial concerns by successfully passing all dynamic (nonlinear, transient, explicit) solutions with no local or global buckling at ultimate loads. This was accomplished by the described design and analysis methods.

The design and analysis approach was validated by drop-testing a 20” diameter subscale titanium orthogrid test article. This test article was first designed and modeled with the developed approach for purposes of validation. Test predictions were also part of the verification process to correlate the results of Nastran’s implicit nonlinear transient solutions and explicit solutions from LS-DYNA. Dynamic drop tests were completed and compared to the converged predictions. The methods were not only validated by the dynamic tests, but the durability of the design was also demonstrated.

A lighter-mass structural concept was developed by a trade analysis which led to a new set of design and analysis procedures undertaken

on the down-selected design. The new process for design and analysis of the orthogrid structure was built upon use of multiple analysis codes, and the novel use of simulation data netted a nearly 50% mass reduction on the baseline design. This far exceeded the original goals of the project by delivering a significant potential mass savings to the Orion program. The sizing procedure accomplished this without compromising on a comprehensive set of failure mode checks.

10. Acknowledgements

The author would like to thank and acknowledge Mike Kirsch of the NASA NESC for providing overall project leadership to the heat shield team, and also Sotiris Kellas of the NASA NESC for assisting with the analysis and leading the testing and verification efforts.

11. References

Roark, Raymond J., Warren C. Young, and Richard G. Budynas. *Roark's Formulas for Stress and Strain*. New York: McGraw-Hill, 2002. 840.

HyperSizer Help Documentation, v7.0, Collier Research Corporation

http://www.nasa.gov/exploration/systems/mpcv/explore.html